Modelling pellet flow in single extrusion with DEM

O P Michelangelli[1], **M Yamanoi**[2], **A Gaspar-Cunha**[1], and **J A Covas**[1]*
[1]Institute for Polymers and Composites/I3N, University of Minho, Guimarães, Portugal
[2]Department of Macromolecular Science and Engineering, Case Western Reserve University, Cleveland, Ohio, USA

The manuscript was received on 14 November 2010 and was accepted after revision for publication on 6 July 2011.

DOI: 10.1177/0954408911418159

Abstract: Plasticating single-screw extrusion involves the continuous conversion of loose solid pellets into a pressurized homogeneous melt that is pumped through a shaping tool. Traditional analyses of the solids conveying stage assume the movement of an elastic solid plug at a fixed speed. However, not only the corresponding predictions fail considerably, but it is also well known that, at least in the initial screw turns, the flow of loose individual pellets takes place. This study follows previous efforts to predict the characteristics of such a flow using the discrete element method. The model considers the development of normal and tangential forces resulting from the inelastic collisions between the pellets and between them and the neighbouring metallic surfaces. The algorithm proposed here is shown to be capable of capturing detailed features of the granular flow. The predictions of velocities in the cross- and down-channel directions and of the coordination number are in good agreement with equivalent reported results. The effect of pellet size on the flow features is also discussed.

1 INTRODUCTION

Most polymer processing technologies encompass a plasticating step where the inward solid pellets are conveyed forward, the system is melted and melt mixed, and then pumped through a shaping tool. Given its practical importance, this operating unit has attracted extensive theoretical and experimental research. As a result, by the 1980s, the underlying thermal, physical, and rheological phenomena were well identified, understood, and could be satisfactorily modelled from hopper to die exit [**1**, **2**]. For this purpose, the plasticating sequence is usually analysed as a series of individual stages where distinct phenomena develop and whose frontiers are delimited by boundary conditions that ensure global coherence. The stages usually comprise: gravity flow in the hopper, drag solids conveying, delay in melting, melting, melt conveying, and die flow [**3**]. The mathematical description of each stage may vary from simple analytical expressions to complex numerical three-dimensional (3D) models. Nevertheless, in most cases, solids conveying is simply described as the drag flow of a cohesive elastic plug moving between flat walls with known friction coefficients. The original analysis was developed by Darnell and Mol [**4**], who performed force and torque balances on an elementary plug slice and obtained a direct relationship between output and pressure development. However, output predictions may be rather poor, with much higher predicted than measured pressure development [**5**]. In fact, there is strong evidence that, at least in the initial screw turns, the assumption of a plug is far from accurate:

1. When performing Maddock-type experiments [**6**] involving the sudden interruption of steady extrusion, the decoupling of the die and the quick extraction of the screw, the material deposited in the first few turns is lost, as it consists of loose pellets (see examples of results of these experiments in Tadmor and Klein [**7**]), while the remaining forms a more or less consistent helix.

*Corresponding author: Institute for Polymers and Composites/I3N, University of Minho, Guimarães 4800-058, Portugal.
email: jcovas@dep.uminho.pt

2. The occurrence of throughput fluctuations or of difficulties with the inflow behaviour of the pellets with increasing screw speed is often related to conveying problems that are difficult to explain with the presence of a solid plug [**8**].
3. Visualization studies making use of single-screw extruders fitted with observation windows have recurrently reported that, at least for some screw geometries, the material in the solids conveying section is only loosely packed [**9**] or that melting occurs before a solid plug is formed [**10**, **11**].

Fang *et al.* [**5**] developed a non-plug solid conveying theory where the pellets progress down-channel at different speeds. The authors considered a linear elastic system that can only resist compressive forces and used the finite element method (FEM) to determine the relationship between internal stress and velocity profile. However, not only the equivalence between the FEM mesh and the physical pellets is not obvious, but the model also requires *a priori* information of the movement of the solids.

Potente and Pohl [**8**] assumed that the flow of plastic pellets in the first section of the single-screw extruder can be divided into three zones: (a) hopper; (b) inflow zone beneath the hopper without pressure build-up; and (c) conveying zone with pressure build-up. In principle, the first and the last could be modelled using the available conventional approaches [**4**, **12**]. Considering the experimental observations reported above, the second zone may well extend along more screw turns. The challenge here is not only to describe adequately the flow characteristics, but also to identify the location of the transition between zones (a) and (b).

In the past decade, research on the flow of granular materials has become particularly active. Even the response of a bulk system of cohesiveless pellets to perturbations can be very complex, with the interactions dominated by contact forces originating from collision and friction [**13**–**16**]. Studies of the flow of granular matter due to plane and annular shear, vertical chutes, inclined planes, or rotating drums have been reported [**17**]. The first attempts to model granular flow in the initial screw turns of a single-screw extruder were made by Potente and Pohl [**8**] (2D approach) and Moysey and Thompson [**18**–**20**] (3D analysis), who used the discrete element method (DEM) and took into account the interaction between individual particles and between the latter and the screw and barrel walls, thus predicting the position and velocities of every pellet. Moysey and Thompson [**18**–**20**] showed the influence of the screw flights on the velocity profiles and that the pellets tend to concentrate at the central channel region. More recently, Yung *et al.* [**21**] adopted a similar approach to model the flow of solids along an inclined microplasticating unit.

The above efforts also demonstrated the potential of DEM to elucidate the flow dynamics and structure of solid pellets in the initial turns of a screw extruder, before heat and pressure eventually bring about the formation of a plug. Thus, this study is part of a broader effort to extend these earlier efforts and investigate the role of process parameters on the flow characteristics. The algorithm presented computes the individual velocity profiles, global output rate, coordination number, and the evolution of density/packing fraction (the variation of this density with time is often designated as 'solids pulsing' [**19**]).

This article is organized as follows. In Section 2, the DEM model is presented and described in detail. Section 3 is devoted to model validation and presentation and discussion of density profiles. Section 4 examines the effect of average pellet size on the dynamics of the granular flow. Finally, Section 5 contains the main conclusions of this study.

2 SIMULATION METHODOLOGY

2.1 Discrete element method

The DEM is a computational tool suitable to model the flow of granular materials. The interested reader is referred to the recent review prepared by Zhu *et al.* [**22**] for an overview of the technique and its applications. Figure 1 depicts the flowchart of the program developed (in C++ language) by the authors. As other DEM algorithms, it typically comprises three main steps [**23**]:

1. A sub-grid method is used to build a near-neighbour interaction list containing all pairs of particles that have a probability of colliding. This list is used to reduce the calculation time required to detect the contacting pairs.
2. If a collision between particles and/or with the boundaries occurs, the forces and torques calculated for those iterations are recalculated.
3. The equations of motion resulting from the previous step are integrated using a second-order predictor–corrector scheme [**23**]. This enables the calculation of the particle velocities and positions in each time step.

Since in DEM each moving particle is individually considered [**18**, **20**], it is necessary to model all collisions between particles and between them and their environment.

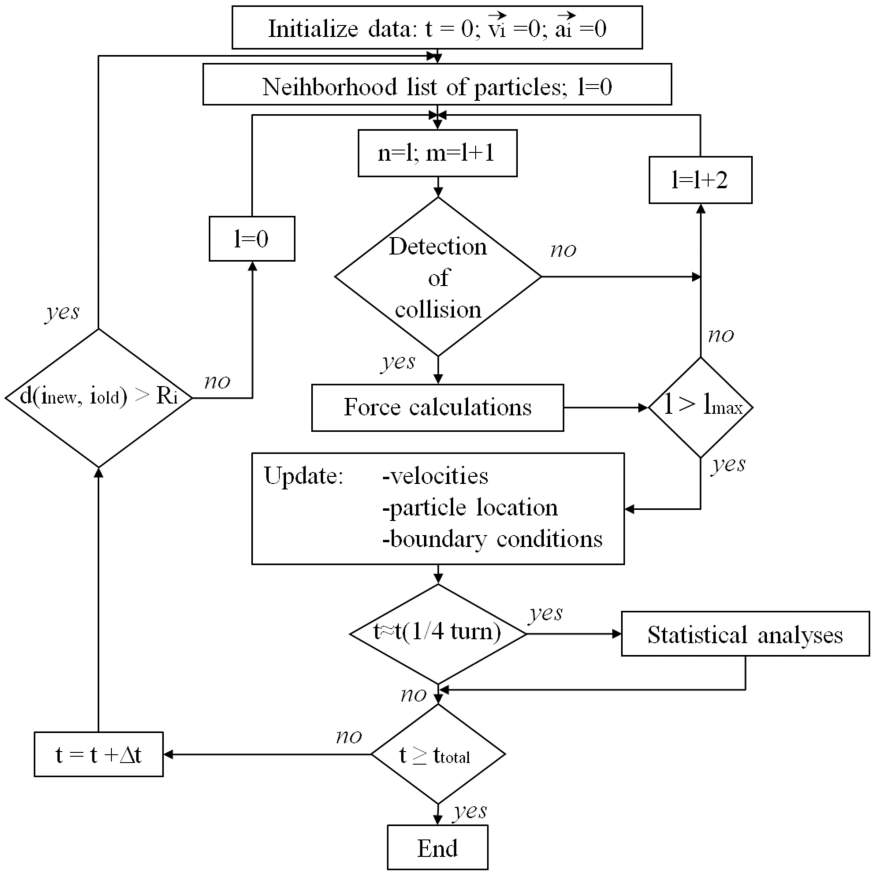

Fig. 1 Flowchart of the DEM algorithm

All the calculations related with interactions are made at fixed time steps. Thus, the time step chosen must be lower than that needed for the interactions to take place. Initially, the particle velocity and acceleration are set to zero. A near-neighbourhood list ($l = 0, 1, \ldots, l_{max}$) of the possible pairs of particles to come in contact with each other is generated using the sub-grid method. In this list, the probable interaction occurs between particles l and $l+1$ (for $l = 0, 2, \ldots, l_{max} - 1$). Then, the occurrence of collisions between particles l and $l+1$ is tested. Simultaneously, the possible collision between all particles and the boundaries (i.e. the screw/barrel walls) is also examined. When a (particle–particle and/or particle–wall) collision takes place, the resulting forces are calculated for the particles involved. After checking the entire neighbourhood list and all the possible collisions between particles and walls, the velocities, particle location, and boundary conditions are updated. Periodically (more specifically, after each time step corresponding to a screw rotation of 90°), a complete analysis of the entire geometrical system is performed. This includes the calculation of output, density profile, velocity profiles, and coordination number. If the current calculation time (t) is smaller than the total calculation time (t_{TOTAL}) defined initially, it is increased by the time step (Δt) and the calculation procedure continues. Then, the near-neighbourhood list is refreshed if the maximum distance between the particles is higher than the particle radius. If so, the position of each particle in the last refresh is saved and compared with its current position.

2.2 Model for granular flow

The model of granular flow in an extruder screw considers the existence of spherical particles whose resistance to overlap is expressed in terms of a continuous potential function [**24**, **25**]. Taking into consideration the good results obtained by Moysey and Thompson [**18**] for the collision of high-density polyethylene (HDPE) pellets assuming plastic deformation, the Walton and Braun (WB) [**26**] model was adopted. Figure 2 illustrates a pair of spherical particles i and j, with radius R_i and R_j, respectively, which are in contact. The value of the overlap (α) can be defined as $\alpha = R_i + R_j - |\vec{r}_{ij}|$, where $\vec{r}_{ij} = |\vec{r}_{ij}|\hat{n}$ is the vector

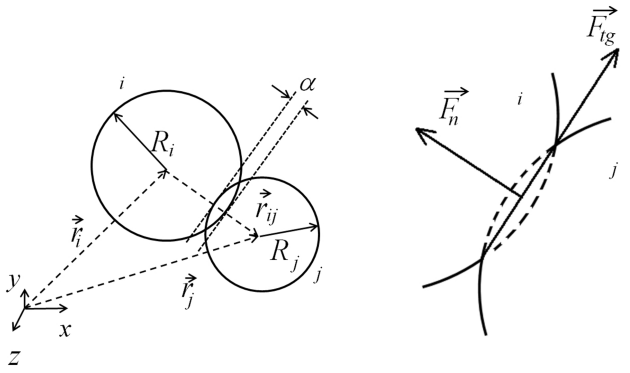

Fig. 2 Schematic representation of the interaction between two particles *i* and *j*

connecting the centres of the *i*th and *j*th particles and $\hat{n}$ the unit vector in that direction. The WB model is used to calculate the normal force ($\overrightarrow{F_n}$) by assuming the existence of two different spring constants, k_1 and k_2, for the loading and unloading forces during the contact, respectively

$$\overrightarrow{F_n} = \begin{cases} k_1(\alpha - \alpha_0)\hat{n}, & \textit{for loading} \\ k_2\alpha\hat{n}, & \textit{for unloading} \end{cases} \quad (1)$$

where α_0 is the value of α when the normal force becomes zero during unloading, in the case of an inelastic regime.

Figure 3 represents the force–displacement relationship during the interaction between two particles. When these start to interact (for example, due to the velocities imposed previously), the initial loading takes place along line 'ab', with a slope of k_1. If unloading is initiated before reaching the point 'b', the interaction follows the path 'ba' (elastic regime). However, if it reaches (or surpasses) the point 'b', the interaction will follow the line 'bd' with a slope of k_2 and then move to the point 'a' (inelastic regime). If the applied normal force increases again after reaching the point 'a', the force–displacement response will follow the pathway 'adbc' and subsequent unloading follows the lines 'ceda'. If a normal force is again applied, it will follow the sequence 'adec'. Path 'ab' is only followed when the interaction begins [**26**].

Therefore, to compute the normal force due to the contact between two particles, it is necessary to preserve the historical data of the forces developed at each of the previous contacts. The inelastic regime applies when the normal force is zero, i.e. when the particles follow the 'ad' or 'ae' lines. This normal force causes a collision with a coefficient of restitution (e_n) that is independent of the relative particles velocity

$$e_n = \sqrt{\frac{k_1}{k_2}} \quad (2)$$

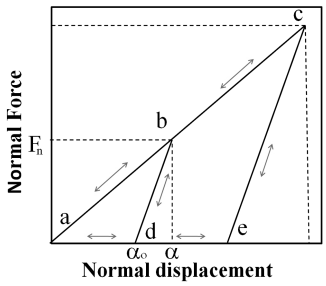

Fig. 3 Graphical representation of the force–displacement hysteresis during the interaction between two particles

In addition, the model is used for the calculation of the tangential forces, which are also dependent on the force–displacement historical data. The tangential displacement parallel ($\Delta\overrightarrow{s_\parallel}$) and perpendicular ($\Delta\overrightarrow{s_\perp}$) to the tangential force are considered separately. The tangential force ($\overrightarrow{F_{tg}}$) is defined as a function of the previous tangential force ($\overrightarrow{F^*_{tg}}$)

$$\overrightarrow{F_{tg}} = \overrightarrow{F^*_{tg}} + K_t\Delta\overrightarrow{s_\parallel} + k_o\Delta\overrightarrow{s_\perp} \quad (3)$$

where K_t is the effective tangential stiffness in the parallel direction, given by

$$K_t = \begin{cases} k_o\left(1 - \dfrac{F_{tg} - F^*_{tg}}{\mu F_n - F^*_{tg}}\right)^\gamma, & \textit{when } F_{tg} \textit{ increases} \\ k_o\left(1 - \dfrac{F^*_{tg} - F_{tg}}{\mu F_n + F^*_{tg}}\right)^\gamma, & \textit{when } F_{tg} \textit{ decreases} \end{cases} \quad (4)$$

In this equation, k_o is the initial tangential stiffness, F_{tg} and F^*_{tg} the magnitudes of the current and previous tangential forces (the latter is set to zero when the contact starts), μ the friction coefficient, and γ an empirical constant (taken as 0.33; if set to zero, the model becomes linear). The effective tangential contact stiffness decreases with the tangential displacement. Also, full sliding develops when the applied tangential forces are higher than the limit of the Coulomb friction forces (i.e. μF_n).

The parallel ($\Delta\overrightarrow{s_\parallel}$) and perpendicular ($\Delta\overrightarrow{s_\perp}$) displacements depend on the total displacement during an 'half-step' (identified with the index $-\frac{1}{2}$), before the required correction in the Verlet velocity integration algorithm [**19**]

$$\Delta\overrightarrow{s_\parallel} = \left(s^{t-\frac{1}{2}} \cdot \hat{t}\right)\hat{t} \quad (5)$$

$$\Delta\overrightarrow{s_\perp} = \Delta s^{t-\frac{1}{2}} - \Delta\overrightarrow{s_\parallel} \quad (6)$$

In these equations, $\hat{t}$ is the unit vector of the current friction force $\overrightarrow{F_{tg}}$, and the relative surface

displacement ($\Delta s^{t-\frac{1}{2}}$) is projected onto the contact tangent plane

$$\Delta s^{t-\frac{1}{2}} \approx \Delta\vec{r}_{ij} - \hat{r}_{ij}\left(\hat{r}_{ij}\cdot\Delta\vec{r}_{ij}\right) + \left[R_i\left(\vec{\omega}_i^{\,t-\frac{1}{2}}\times\hat{r}_{ij}\right) + R_j\left(\vec{\omega}_j^{\,t-\frac{1}{2}}\times\hat{r}_{ij}\right)\right]\Delta t \tag{7}$$

where $\Delta\vec{r}_{ij} = \vec{r}_{ij}^{\,n} - \vec{r}_{ij}^{\,n-1}$ is the change in the relative position vector during the preceding time step and $\vec{\omega}$ the particle angular velocity. The unit vector $\hat{t}$ is calculated from the tangential forces in the preceding time step ($\overrightarrow{F_{tg}^{*}}$). For that purpose, $\overrightarrow{F_{tg}^{*}}$ is projected onto the current tangent plane, yielding

$$\overrightarrow{F_o} = \overrightarrow{F_{tg}^{*}} - \hat{r}_{ij}\left(\hat{r}_{ij}\cdot\overrightarrow{F_{tg}^{*}}\right) \tag{8}$$

In turn, this projected friction force is normalized to the old magnitude as

$$\overrightarrow{F'_{tg}} = \left|\frac{\overrightarrow{F_{tg}^{*}}}{\overrightarrow{F_o}}\right|\overrightarrow{F_o} \tag{9}$$

and the unit vector is given by

$$\hat{t} = \frac{\overrightarrow{F'_{tg}}}{\left|\overrightarrow{F'_{tg}}\right|} \tag{10}$$

Finally, the value of the friction force at the current time step ($\overrightarrow{F_{tg}}$) can be obtained from equation (3).

2.3 Extruder geometry

During flow of the pellets in the initial screw turns, it is necessary to consider the following boundary conditions where contacts can/will take place: (a) the walls of the hopper; (b) the rim between the hopper aperture and the barrel, (3) the internal barrel wall, (4) the screw flights, (5) the flights crest (below the hopper entrance), (6) the edge between the screws flights and crest, and (7) the screw root. No leakage flow between the screw flights and the inner barrel wall exists due to the small value of the mechanical gap in comparison with the size of the pellets.

The extruder geometry is illustrated in Fig. 4, together with the initial location of the pellets in the hopper. As the screw (flights and root walls) rotates and flow develops, new layers of pellets are appended to the hopper. However, gravity flow in this element is not included in the simulations.

Figure 5(a) represents the decomposition of the forces arising when the pellets interact with the barrel and screw root walls, which happens when $R_{xy} - d/2 < R_{int}$ and $R_{xy} + d/2 > R_{ext}$ (R_{xy} is the projection on the xy plane of the distance vector screw centre to pellet and d the pellet diameter), respectively. These forces are calculated from equations (1) and (3). However, in order to apply the latter, one first needs to apply equation (7). In this equation, i will be considered to be either the barrel or the screw and j the pellet. In the case of the barrel, the term involving R_i is nil since the angular velocity ($\vec{\omega}_i^{\,t-\frac{1}{2}}$) is also nil; for the screw, R_i becomes R_{int} and the angular velocity is now the screw speed.

Due to the possible contacts, the screw pushing and trailing flights must be described separately. The geometry of the former may be expressed by

$$r(\theta) = R\cos\theta\hat{\boldsymbol{i}} + R\sin\theta\hat{\boldsymbol{j}} + \frac{P}{2\pi}\theta\hat{\boldsymbol{k}} \tag{11}$$

where R is the distance between the contact point on the wall (z_c) and the screw axis, P the pitch, and θ a parametric variable. The parametric variable, θ'_3, at

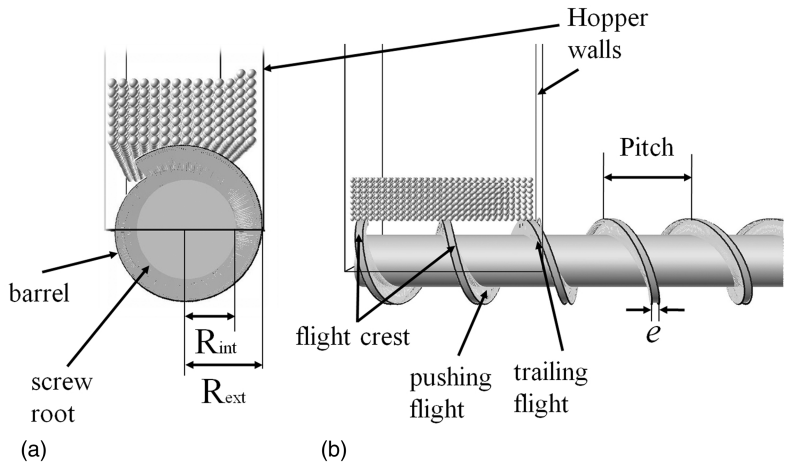

Fig. 4 Extruder geometry and initial position of the pellets in the hopper

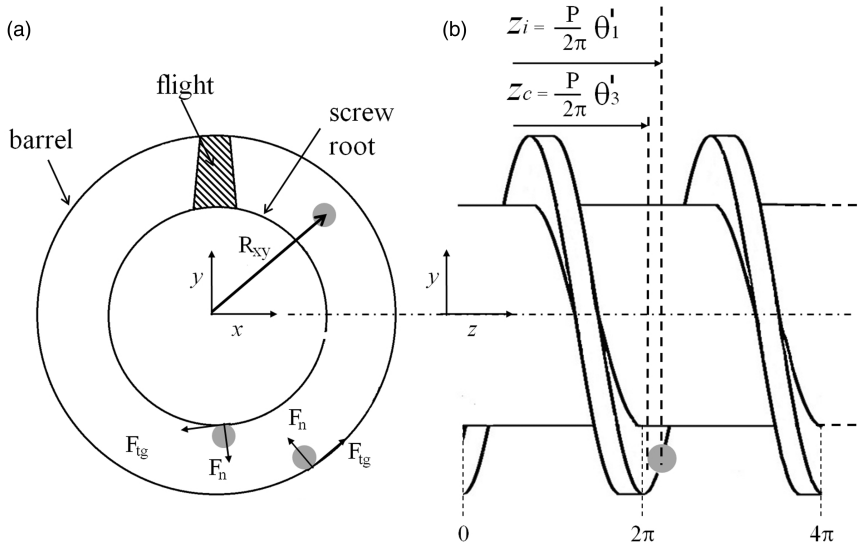

Fig. 5 Schematic representation of the screw channel: (a) transversal cross-section showing the interaction between the barrel/screw root walls and the pellets; (b) side view detailing the contact between one pellet and the pushing flight

the contact point between the pushing flight and the pellet is defined as

$$\theta_3' = \theta_1' + 2\sin^{-1}\left(\frac{d_1}{2R_{xy}}\right)\left(sin^2\phi - 1\right) \tag{12}$$

where

$$\phi = \tan^{-1}\left(\frac{P}{2\pi R_{xy}}\right) \tag{13}$$

$\theta_1' = 2\pi^* z_i/P$ is determined from the z-position of the pellet and d_1 relates the position of the pellet with the contact point on the surface of the pushing flight

$$d_1 = \sqrt{\left\{\begin{array}{l}\left(x_i - R_{xy}\cos\left(\theta_1' - \theta_N\right)\right)^2 \\ \quad +\left(y_i - R_{xy}\sin\left(\theta_1' - \theta_N\right)\right)^2\end{array}\right\}} \tag{14}$$

with $\theta_N = 2\pi\omega t$. The trailing flight is defined by

$$\vec{r}(\theta+\theta_e) = R\cos(\theta+\theta_e)\hat{\boldsymbol{i}} + R\sin(\theta+\theta_e)\hat{j} + \frac{P}{2\pi}(\theta+\theta_e)\hat{\boldsymbol{k}} \tag{15}$$

where θ_e represents its thickness

$$\theta_e = 2\sin^{-1}\left(\frac{e}{2^*\sin(\oslash)R_{xy}}\right) \tag{16}$$

The distance between the centre of the pellet and the trailing flight at a z-distance is calculated from

$$d_1 = \sqrt{\left\{\begin{array}{l}\left(x_i - R_{xy}\cos\left(\theta_1'' - \theta_N + \theta_e\right)\right)^2 \\ \quad +\left(y_i - R_{xy}\sin\left(\theta_1'' - \theta_N + \theta_e\right)\right)^2\end{array}\right\}} \tag{17}$$

Thus, the contact point of the trailing flight with the pellet is identified from

$$\theta_3'' = \theta_1'' + 2\sin^{-1}\left(\frac{d_1}{2R_{xy}}\right)\left(1 - sin^2\phi\right) \tag{18}$$

To represent the pellet interaction, a helical coordinate system is adopted [**27**, **28**]

$$\begin{bmatrix}\vec{\boldsymbol{e}}_r \\ \vec{\boldsymbol{e}}_l \\ \vec{\boldsymbol{e}}_w\end{bmatrix} = \begin{bmatrix}R\cos\theta & R\sin\theta & 0 \\ \tau\sin\theta & -\tau\cos\theta & \kappa \\ \kappa\sin\theta & -\kappa\cos\theta & -\tau\end{bmatrix}\begin{bmatrix}\hat{\boldsymbol{i}} \\ \hat{\boldsymbol{j}} \\ \hat{\boldsymbol{k}}\end{bmatrix} \tag{19}$$

where κ is the curvature and τ the torsion of the helix

$$\kappa = \frac{R}{\sqrt{R^2 + \left(\frac{P}{2\pi}\right)^2}} \tag{20}$$

$$\tau = \frac{\left(\frac{P}{2\pi}\right)^2}{\sqrt{R^2 + \left(\frac{P}{2\pi}\right)^2}} \tag{21}$$

The location of the pellets is defined by equation (19) replacing θ by θ_3' or θ_3' for the pushing and trailing flights, respectively.

Finally, it is also necessary to define the flight crest, as the pellets interact with it in the hopper opening. The contact conditions are identified by the pellets' z-coordinate and position in the xy plane. A potential collision of pellets with the flight crest occurs if $z_i < \left(\frac{P}{2\pi}\right)(\theta_1 - \theta_N)$ and $z_i > \left(\frac{P}{2\pi}\right)(\theta_1 - \theta_N - \theta_e)$, and when the pellet obeys the condition $R_{xy} + d/2 > R_{\text{ext}}$.

2.4 Dimensionless parameters

The computations were carried out considering the dimensionless parameters presented in Table 1. They were defined as a function of mass (m), gravity acceleration (g), and diameter (d).

3 MODEL VALIDATION

3.1 Simulation parameters

The above algorithm can be validated by comparing its predictions of output, velocity profile, and coordination number with those reported in the literature for the same case study [**18**, **20**]. Additionally, due to its practical importance, the packing fraction will also be computed.

Table 2 presents the extruder geometry and the properties of a HDPE homopolymer, with a density of 945 kg/m^3, available in pellets with an average diameter of 3 mm. The barrel of the extruder has an internal diameter of 50.8 mm and a length-to-diameter (L/D) ratio of 30:1. However, only the seven initial turns were considered in the simulations, as just granular flow is being studied. The data are as similar as possible to that used by Moysey and Thompson [**18**, **20**], in order to allow a direct comparison with the results there in. The dimensionless values were determined considering $g = 1\,\text{m/s}^2$, $m = 1.34\text{e}^{-5}$ kg and $d = 3$ mm.

It is assumed that the screw channel is initially fully filled with pellets. This was achieved by setting the screw speed to 100 r/min and adding 840 particles to the hopper per 90° of screw rotation. As shown in the sequence represented in Fig. 6(a) to (f), each corresponding to a period of 0.5 s of flow, the channel is progressively filled until a total of 25 000 particles are involved. The screw is stopped and this will now become the initial condition for all the subsequent simulations. This procedure assures that all the computations are independent of the variation of any random parameter, as the initial conditions are always the same. Accordingly, the results are reproducible and only change when a modification to the initial data in Table 2 is made.

Table 3 presents the computational experiments carried out, which were designed to illustrate the effect of screw speed. In all cases, open discharge conditions were adopted (i.e. absence of any restriction downstream). A time step of 10^{-5} s was used. The output rate was estimated by counting the number of pellets passing through the screw cross-section at 4.5 L/D. The velocity profiles in the x-, y-, and z-directions and the packing fraction were determined as average values, taking into consideration the particles contained in a differential volume, as shown in Fig. 7. This volume corresponds to 0.30 rad (17°) measured at the screw root, which is equivalent to *ca* 1.5 times the diameter of a particle. The coordination number was calculated using the near-neighbourhood list, by comparing the distances between the pellets and taking into account the number of contacts during the corresponding flow time (Table 3).

Table 1 Dimensionless parameters

Parameter	Dimensionless form	
Mass	$m^* = \frac{1}{m} m$	(22)
Gravity	$g^* = \frac{1}{g} g$	(23)
Distance	$r^* = \frac{1}{d} r$	(24)
Time	$t^* = \sqrt{\frac{g}{d}} t$	(25)
Angular velocity	$\omega^* = \sqrt{\frac{d}{g}} \omega$	(26)
Spring constant	$k^* = \frac{d}{mg} k$	(27)

Table 2 Polymer properties and extruder geometry

	Parameter	Value	Dimensionless value
HDPE	Density of a pellet	945 kg/m^3	1.90
	Mass of a pellet	1.34e−5 kg	1
	External coefficient of friction		
	with barrel	0.28	0.28
	screw	0.25	0.25
	Coefficient of friction between pellets	0.29	0.29
	Stiffness coefficient k_1	375 N/m	83 955
	Coefficient of restitution (ε)	0.5	0.5
Extruder	Barrel diameter (D_b)	50.8 mm	16.9
	Screw channel depth (H)	10.16 mm	3.3
	Flight lead (L)	50.8 mm	16.9
	Flight thickness (e)	5.08 mm	1.69
	Screw axial length	7 L/D	7 L/D

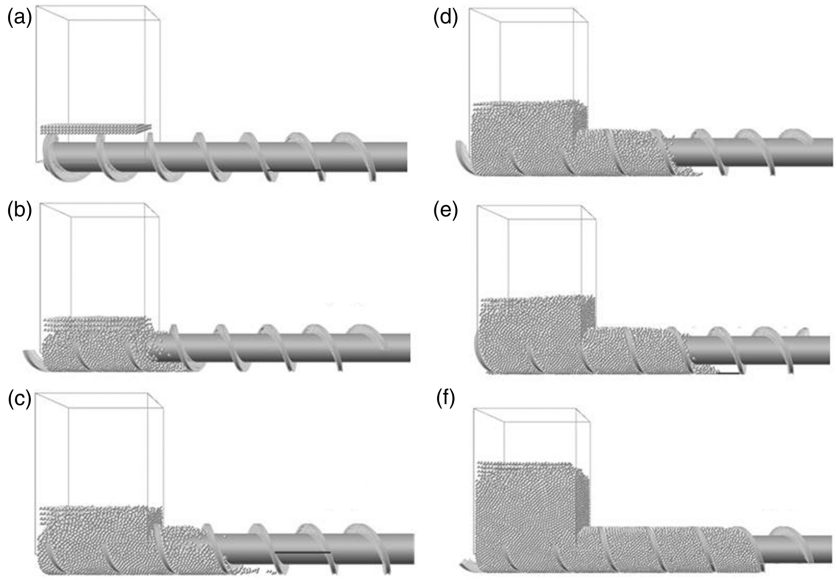

Fig. 6 Sequence of computations performed to ensure that the channel is fully filled at the start-up of any flow simulation (steps shown at flow intervals of 0.5 s, with the screw rotating at 100 r/min)

Table 3 Computational runs performed

Run	Screw speed (r/min)	Flow time (s)
1	10	15
2	20	15
3	30	10
4	50	6
5	100	5
6	150	5
7	180	5

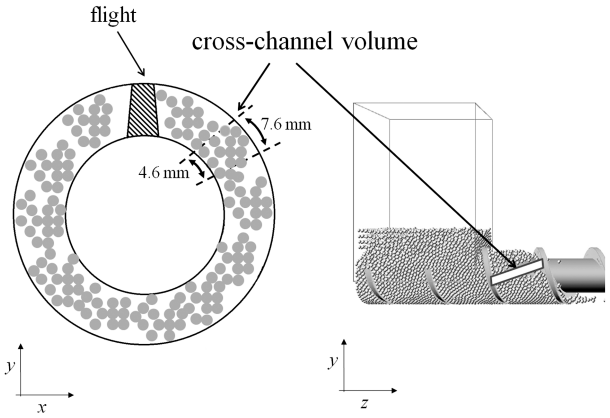

Fig. 7 Schematic representation of the cross-channel volume where the average calculations are made

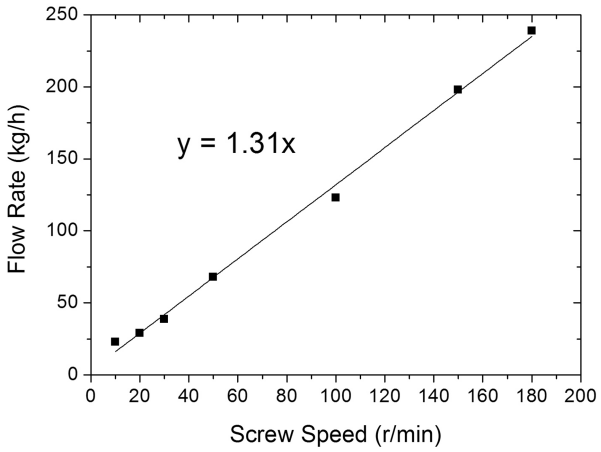

Fig. 8 The effect of screw speed on flowrate

Table 4 Comparison of specific outputs

Model	Specific output (kg/h r/min)
Darnell and Mol [**4**] by [**20**]	1.23
Tadmor and Klein [**7**] by [**20**]	0.93
Moysey and Thompson [**19**, **20**]	1.34
Experimental [**20**]	1.36
This algorithm	1.31

3.2 RESULTS

Figure 8 shows the influence of screw speed on flowrate (runs 1–7 in Table 3). The slope of this linear relationship yields a value of 1.31 kg/h r/min and represents the specific output of the machine. Table 4 compares this value with those produced by two classical plug flow analytical models (Darnell and Mol [**4**] and Tadmor and Klein [**7**]) by the DEM approach of Moysey and Thompson [**19**, **20**] and with an experimental value reported by the Moysey

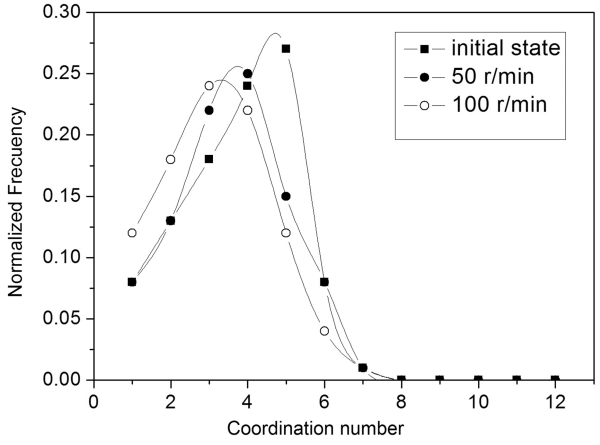

Fig. 9 Coordination number distribution at the initial state ($t = 0$ s) and for two screw speeds (50 and 100 r/min)

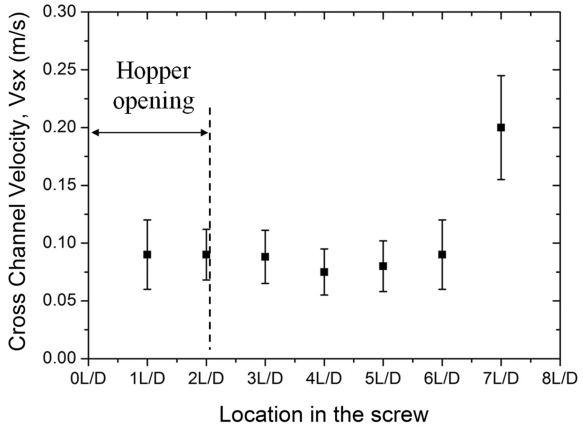

Fig. 10 Axial cross-channel velocity profile at 100 r/min (average obtained during 5 s)

and Thompson [**20**]. The good performance of the DEM methodology is evident. The differences between the two DEM approaches are probably due to the difficulty in defining exactly the same initial conditions for the simulations, as relatively little detail is given in the original papers.

The coordination number can be defined as the average total number of contacts of all particles during the flow. This parameter provides information on the structure developed due to the transport dynamics. Figure 9 shows the distribution function (in terms of a normalized frequency) of the coordination number for two different screw speeds (50 and 100 r/min), the initial state corresponding to $t = 0$. It is clear that the core of the distribution decreases with increasing screw speed, although the shape of the function is maintained. This means that the bulk structure of the granules does not change significantly during the flow. Moysey and Thompson reported identical results [**19**].

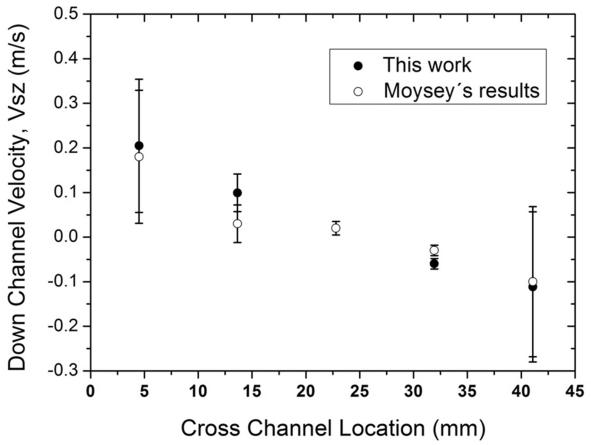

Fig. 11 Down-channel velocity profile at 2.5 L/D at 100 r/min

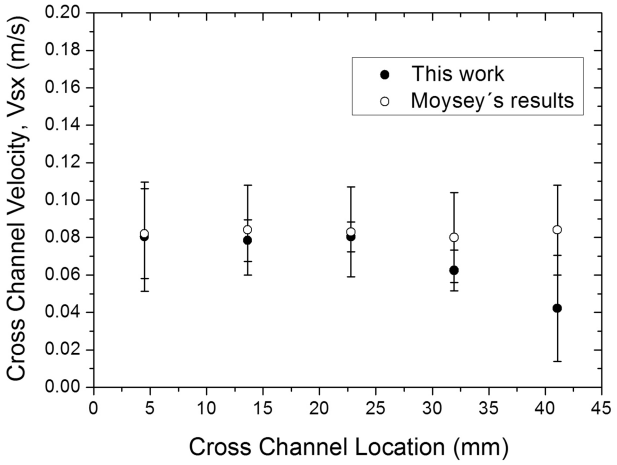

Fig. 12 Cross-channel velocity profile at 2.5 L/D at 100 r/min

The predicted velocity profiles are shown in Figs 10 to 12. Figure 10 shows the evolution of the average cross-channel velocity (V_{sx}) along the screw channel, when the screw rotates at 100 r/min. As anticipated, somewhat higher velocity fluctuations occur under the hopper and towards the screw exit (6–7 L/D). The latter is explained by the open discharge boundary conditions at the exit of the extruder. However, as observed also by Moysey and Thompson [**19**], the variation of the velocities across the channel depth is quite low. Figure 11 plots the average down-channel velocity at 2.5 L/D (after flow during 5 s), again for a screw speed of 100 r/min. As expected, the flow of the pellets is strongly influenced by the presence of the screw flights, the down-channel velocities being positive near to the pushing flight and negative near to the trailing one. The global average velocity is obviously positive. Simultaneously, the cross-channel velocities at same screw location (Fig. 12) are positive.

Thus, a predominately axial positive displacement of the pellets is produced. Figures 11 and 12 show that the differences between the predictions obtained with this algorithm and those reported by Moysey and Thompson [**20**] are small. In fact, the decrease of the cross-channel velocity near to the trailing flight predicted by the method presented here seems more realistic.

3.3 Packing fraction

The evolution of the packing fraction along the screw channel has practical consequences, as it dictates not only the mass output, but also the eventual density fluctuations. Figure 13 shows a typical snapshot at 0.15 s of flow at 100 r/min. Figure 14 shows the cross-channel variation of the packing fraction at 2.5 L/D, for different flow times. At $t=0$ s, variations are small since the pellets are at rest. At $t=2.55$ s, the packing fraction shows a maximum at the channel core, the variations being non-symmetrical towards the side walls. The packing fraction increases for $t=4.95$ s and the shape of the curve attenuates. Although the computational costs are too high to obtain values for a truly operating steady state, one would speculate that the behaviour would converge to a curve similar to that for 4.95 s, as the contacts with the flights drive the pellets towards the channel core, even if distinct at each wall.

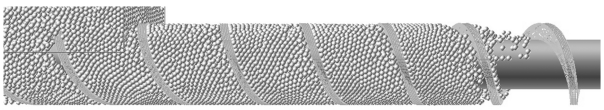

Fig. 13 Typical snapshot during the flow time for 100 r/min screw speed at 0.15 s

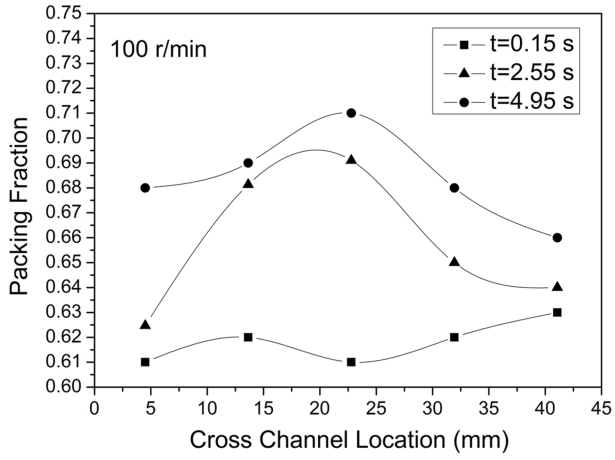

Fig. 14 Cross-channel variation of the packing fraction at 2.5 L/D and 100 r/min

Figure 15 shows the evolution of the packing fraction along the screw channel, again at 100 r/min, for three flow times. No relevant fluctuations take place at the opening of the hopper, probably due to the existing vertical hydrostatic pressure. Beyond this zone, cyclic fluctuations develop with a frequency matching the screw rotation. These are due to the role of gravity in the system, with the packing fraction peaks corresponding to the bottom of the channel. The fluctuations decrease with increasing flow time and range approximately between 0.7 and 0.5, i.e. between close and loose packing, respectively. Interestingly, when the screw operates in open discharge, it becomes progressively less filled in the axial direction. Again, operation under steady-state conditions will probably be similar.

4 EFFECT OF PELLET SIZE

This section analyses the effect of pellet size on the dynamical and structural flow behaviour. The same HDPE was used (see properties in Table 2), but now considering 2, 3, and 4 mm circular pellets, which are within the usual commercial range. The geometry of the available extruder is presented in Table 5, together with the dimensionless values. Data analysis was performed using the same parameters as in Section 3. The same screw pre-filling method was employed, adding 300, 200, or 175 particles, for the 2, 3, and 4 mm particles, respectively. Also, since the spring constant changes with diameter (see equation (27) in Table 1), dimensionless K is set to 1.89e5, 8.39e4, and 4.74e4, respectively.

Table 6 presents the variation of the computational and experimental outputs with screw speed. The experimental data refer to pellets with 3 mm, the

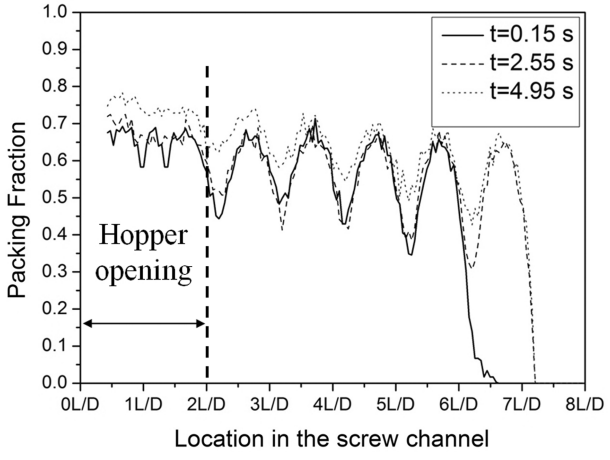

Fig. 15 Evolution of the packing fraction along the screw channel at 100 r/min and for different flow times

Table 5 Extruder geometry

Parameter	Value	Dimensionless value for 2 mm pellet	Dimensionless value for 3 mm pellet	Dimensionless value for 4 mm pellet
Barrel diameter (D_b)	30.0 mm	15	10	7.5
Screw channel depth (H)	5.0 mm	2.5	1.6	1.25
Flight lead (L)	30.0 mm	15	10	7.5
Flight thickness (e)	4.00 mm	2	1.69	1.00
Screw axial length	10 L/D	10 L/D	10 L/D	10 L/D

Table 6 Computational and experimental outputs

	Computational output (kg/h)			
Screw speed (r/min)	$d=2$ mm	$d=3$ mm	$d=4$ mm	Experimental output ($d=3$ mm) (kg/h)
20	1.50	1.48	1.64	1.55 ± 0.06
60	4.58	4.55	4.78	4.66 ± 0.15
80	7.32	7.50	7.70	7.60 ± 0.23
100	9.01	9.20	9.60	9.40 ± 0.14

Table 7 Cross-channel velocity for different screw speeds and pellet sizes at 8 L/D

	Screw speed (r/min)			
Pellet size (mm)	20	60	80	100
2	0.013 ± 0.001	0.026 ± 0.009	0.036 ± 0.004	0.043 ± 0.011
3	0.013 ± 0.004	0.026 ± 0.009	0.037 ± 0.004	0.043 ± 0.011
4	0.014 ± 0.007	0.026 ± 0.010	0.035 ± 0.002	0.043 ± 0.002

Table 8 Down-channel velocity for different screw speeds and pellet sizes at 8 L/D

	Screw speed (r/min)			
Pellet size (mm)	20	60	80	100
2	0.025 ± 0.170	0.105 ± 0.570	0.076 ± 0.710	0.095 ± 0.890
3	0.020 ± 0.220	0.083 ± 0.570	0.081 ± 0.890	0.101 ± 1.120
4	0.020 ± 0.230	0.099 ± 0.640	0.081 ± 0.950	0.101 ± 1.190

ones available for the polymer under study. Although they are more lentil shaped than spherical, differences are smaller than 5 per cent. The table also shows that at constant screw speed, pellet size influences (even if slightly) the output, different trends being observed for the lower and higher screw speed ranges. In fact, while at 20 and 60 r/min, the output for 3 mm pellets is lower than that for 2 mm pellets, at high screw speeds, output increases with increase in pellet size. The reasons for this are not obvious and should be investigated.

Tables 7 and 8 present the average cross- and down-channel velocities at 8 L/D. Although the average values are relatively independent of pellet size (at least no explicit trend is perceived), the high fluctuations of the down-channel velocity are notorious. These fluctuations were discussed above (Fig. 11) and occur near to the screw flights, having a determinant role on flowrate. In the case of Table 8, the standard deviation increases with increasing screw speed to become one order of magnitude higher than the average value, and thus hiding the eventual effect of pellet size. Figures 16 and 17 show the influence of pellet size on the axial profile of the packing fraction after 20 s of flow at 20 and 100 r/min, respectively. The pulsating behaviour is due to the combined effect of gravity and transport. Its amplitude decreases with increasing speed, making the differentiation between the curves for the three pellet sizes much easier at the higher screw speed range. Anyway, as expected, the global degree of compaction decreases with increase in pellet size (see also the average values in Table 9). Therefore, since the dependence of the packing fraction on pellet size and screw speed cannot justify the behaviour observed in Table 6, the explanation has to be in the

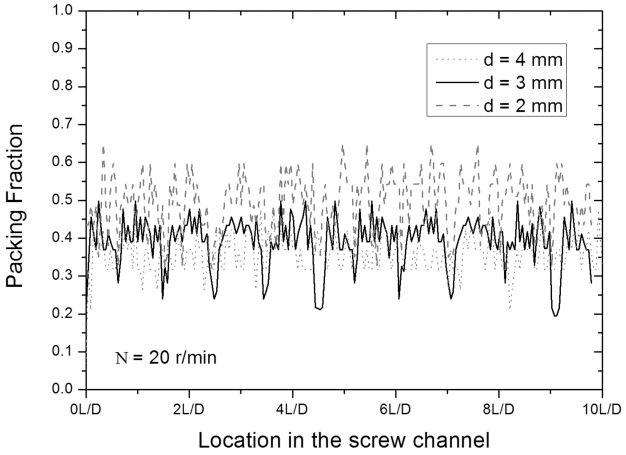

Fig. 16 Influence of pellet size on the axial profile of the packing fraction (20 s at 20 r/min)

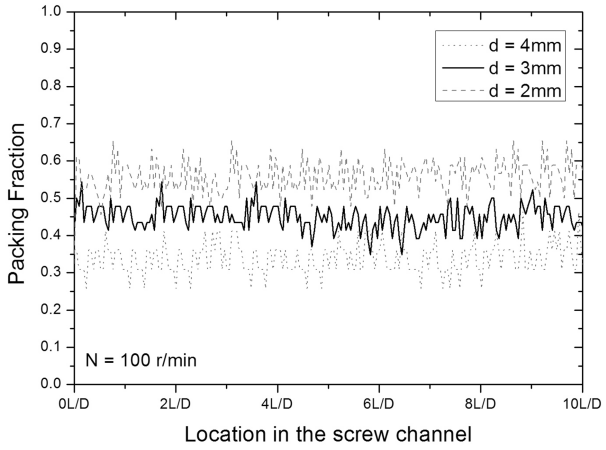

Fig. 17 Influence of pellet size on the axial profile of the packing fraction (20 s at 100 r/min)

values of the down-channel velocity near to the flight walls.

5 CONCLUSIONS

The DEM is used to study the flow of granular matter (typically polymer pellets) in the initial turns of a single-screw extruder. The predictions of flow characteristics such as velocities in the cross- and down-channel directions and coordination number are confronted with equivalent results reported in the literature, a good agreement being obtained.

The DEM model seems to be able to capture detailed features of the granular flow. For example, at a given channel cross-section, the down-channel velocity profile exhibits a significant gradient from the trailing to the pushing flight, with a nil velocity at the centre; conversely, the cross-channel velocities are positive and change little. Therefore, it is not surprising that when comparing output predictions with experiments, DEM simulations show better performance (differences of 1–3 per cent) than analytical analyses assuming the displacement of an elastic solid plug (differences of 10–30 per cent).

Table 9 Average packing fraction for different screw speeds and pellet sizes

	Screw speed (r/min)			
Pellet size (mm)	20	60	80	100
2	0.49 ± 0.07	0.46 ± 0.05	0.55 ± 0.04	0.55 ± 0.04
3	0.39 ± 0.06	0.37 ± 0.08	0.44 ± 0.03	0.45 ± 0.03
4	0.35 ± 0.05	0.36 ± 0.05	0.34 ± 0.05	0.33 ± 0.04

The evolution of the packing intensity of the pellets as flow develops was also investigated. At a given channel cross-section and flow time, a loose packing, denser in the central region, was predicted. Density fluctuations along the channel develop instantly and seem to stay on even if less intense. The algorithm was also sensitive to changes in pellet size, variations both in packing density and output being predicted.

In view of the above, using DEM to model the flow of the pellets in the initial turns of the screw may not only contribute to a better understanding of the transport characteristics in this region, but also to identify the eventual location in the channel where a transition occurs between this flow and the movement of an elastic solid plug generating pressure.

ACKNOWLEDGEMENT

The authors acknowledge the financial support provided by the Portuguese Science Foundation (FCT) under grant SFRH/BPD/39381/2007.

REFERENCES

1 **Tadmor, Z.** and **Gogos, C. G.** *Principles of polymer processing*, edition 2, 2006, p. 447 (John Wiley & Sons, New Jersey).
2 **Rauwendaal, C.** *Polymer extrusion*, edition 2, 1990, p. 222 (Verlag, New York).
3 **Gaspar-Cunha, A.** *Modelling and optimisation of single screw extrusion*. PhD Thesis, University of Minho, Guimarães, 2000.
4 **Darnell, W. H.** and **Mol, E.** Solids conveying in extruders. *SPE J.*, 1956, **12**, 20–29.
5 **Fang, S., Chen, L.,** and **Zhu, F.** Studies on the theory of single screw plasticating extrusion. Part II: Non-plug flow solid conveying. *Polym. Eng. Sci.*, 1991, **31**, 1117.
6 **Maddock, B. H.** A visual analysis of flow and mixing in extruder screws. *SPE J.*, 1959, **15**, 383–389.

7 **Tadmor, Z.** and **Klein, I.** *Engineering principles of plasticating extrusion*, edition 1, 1978 (Krieger Publishing, New York).
8 **Potente, H.** and **Phol, T. C.** Polymer pellet flow out of the hopper into the first section of a single screw. *Intern. Polym. Process.*, 2001, **17**, 11–21.
9 **Wong, A. C.-Y., Liu, T., Lam, J. C. M.,** and **Zhu, F.** Dynamic performance of single-screws of different configurations. *Intern. Polym. Process.*, 1999, **14**, 35–43.
10 **Gao, F., Jin, Z.,** and **Chen, X.** A transparent barrel for study of reciprocating screw injection molding. SPE Technical Papers, *ANTEC 2000*, Orlando, Florida, 8–9 May 2000, p. 523.
11 **Zhu, F.** and **Chen, L.** Studies on the theory of single screw plasticating extrusion. Part I: A new experimental method for extrusion. *Polym. Eng. Sci.*, 1991, **31**, 1113–1116.
12 **Walker, D. M.** An approximate theory for pressures and arching in hoppers. *Chem. Eng. Sci.*, 1966, **21**, 975–997.
13 **De. Gennes, P. G.** Reflections on the mechanics of granular matter. *Phys. A*, 1998, **261**, 267–293.
14 **Duran, J.** *Sand, powder and grains*, 1999 (Springer-Verlag, New York).
15 **Darias, J. R., Sánchez, I.,** and **Gutiérrez, G.** Vertical granular transport in a vibrated U-tube. In conference proceedings of *Traffic and Granular Flow'07*, Paris, 20–22 June, p. 545.
16 **Pozo Michelangelli, O.** and **Olivi-Tran, N.** Effects of elasticity on the shape of measured shear signals in a two-dimensional assembly of disks. *Multi. Model. Mater. Struct.*, 2008, **4**, 179–188.
17 **MiDi, G. D. R.** On dense granular flow. *Eur. Phys. J. E*, 2004, **14**, 341.
18 **Moysey, P. A.** and **Thompson, M. R.** Determining the collision properties of semi-crystalline and amorphous thermoplastics for DEM simulations of solids transport in an extruder. *Chem. Eng. Sci.*, 2007, **62**, 3699–3709.
19 **Moysey, P. A.** and **Thompson, M. R.** Modeling the solids inflow and solids conveying of single-screw extruders using the discrete element method. *Powder Technol.*, 2005, **153**, 95–107.
20 **Moysey, P. A.** and **Thompson, M. R.** Investigation of solids transport in a single-screw extruder using a 3-D discrete particle simulation. *Polym. Eng. Sci.*, 2004, **44**, 2203.
21 **Yung, K. L., Xu, Y.,** and **Ng, H. P.** Modelling method for studying solid conveying process in inclined plastication unit. *Plast. Rubber Compos.*, 2007, **36**, 56–61.
22 **Zhu, H., Zhou, Z., Yang, R.,** and **Yu, A.** Discrete particle simulation of particulate systems: theoretical developments. *Chem. Eng. Sci.*, 2007, **62**, 3378–3396.
23 **Rapaport, D. C.** *The art of molecular dynamics simulation*, 2004 (Cambridge University Press, Cambridge).
24 **Dury, C. M.** and **Ristow, G. H.** Radial segregation in a two-dimensional rotating drum. *J. Phys. I France*, 1997, **7**, 737–745.
25 **Haff, P. K.** and **Werner, B. T.** Computer simulation of the mechanical sorting of grains. *Powder Technol.*, 1986, **48**, 239–245.
26 **Walton, O. R.** and **Braun, R. L.** Viscosity, granular-temperature, and stress calculations for shearing assemblies of inelastic, frictional disks. *J. Rheol.*, 1986, **30**, 949–980.
27 **Germano, M.** On the effect of torsion on a helical flow. *J. Fluid Mech.*, 1981, **125**, 1–8.
28 **Yu, Q.** and **Hu, G.-H.** Development of a helical coordinate system and its application to analysis of polymer flow in screw extruders. Part I: The balance equations in a helical coordinate system. *J. Non-Newtonian Fluid Mech.*, 1997, **69**, 155–167.

APPENDIX

Notation

d	pellet diameter
e	flight thickness
e_n	constant coefficient of restitution of a particle
$\vec{e}_r$, $\vec{e}_l$, $\vec{e}_w$	units vectors of Germano's coordinates
$\overrightarrow{F'_{\mathrm{o}}}$	normalized previous tangential force
$\overrightarrow{F_{\mathrm{n}}}$	normal force between the ith and jth particles
$\overrightarrow{F_{\mathrm{tg}}}$	tangential force between the ith and jth particles
$\overrightarrow{F^*_{\mathrm{tg}}}$	tangential force in previous time step between the ith and jth particles
g	gravity force
i, j	index of ith and jth particles
k_1, k_2	different spring constants of the normal force model
l	index of neighbourhood list
m	mass of the particle
$\hat{\boldsymbol{n}}$	unit vector in the direction of $\vec{\boldsymbol{r}}_{ij}$
P	screw pitch
$\vec{\boldsymbol{r}}_{ij} = \mathrm{v}$	vector connecting the centres of the ith and jth particles
R	distance between the contact point on the wall and the screw axis
R_{int}	radius of the screw root
R_{ext}	barrel radius
R_i, R_j	radius of the ith and jth particles
R_{xy}	projection of the distance vector in the plane xy
t_{TOTAL}	total calculation time increased by the time step (Δt)
$\hat{\boldsymbol{t}}$	unit vector of the friction force $\overrightarrow{F_{\mathrm{tg}}}$
x_i, y_i, z_i	coordinates of the position for the ith particle.
z_{c}	contact point of the pellet in the flight wall
Z	coordination number

α	overlap between *i*th and *j*th particles when interaction occurs
α_0	value of α when the normal force becomes zero during unloading
$\Delta\vec{\boldsymbol{r}}_{ij}$	vector difference between the displacement vectors before and after the last time step
$\Delta\overrightarrow{\boldsymbol{s}_{\parallel}}$	parallel displacement of the friction force
$\Delta\overrightarrow{\boldsymbol{s}_{\perp}}$	perpendicular displacement of the friction force
$\Delta\boldsymbol{s}^{t-\frac{1}{2}}$	projection of the relative surface displacement during the last time step onto the contact tangent plane
Δt	time step
θ	parametric variable
ϕ	helix angle
θ_3^{00B4}, θ_3''	parametric variable representing the point of contact between the flights
θ_1', θ_1''	parametric variable represented by the z-position of the *i*th pellet
θ_e	parametric variable corresponding to the thickness of the flight *e*.
θ_N	parametric variable that represents the cumulative rotation of the screw
κ	helix curvature
μ	static friction coefficient
τ	torsion of the helix
ω,N	angular velocity of the screw or screw speed.
$\vec{\omega}_i^{\,t-\frac{1}{2}}$	the particle angular velocity during the 'half-step' before the correction in the Verlet algorithm.